INL/JOU-22-69401-Revision-0

Comparing Structure-Property Evolution for PM-HIP and Forged Alloy 625 Irradiated with Neutrons to 1 dpa

November 2022

Changing the World's Energy Future

Caleb Clement, Sowmya Panuganti, Patrick H. Warren, Yangyang Zhao, Katelyn Wheeler, David M Frazer, Donna Post Guillen, David W. Gandy, Janelle P. Wharry, Yu Lu

INL/JOU-22-69401-Revision-0

Comparing Structure-Property Evolution for PM-HIP and Forged Alloy 625 Irradiated with Neutrons to 1 dpa

Caleb Clement, Sowmya Panuganti, Patrick H. Warren, Yangyang Zhao, Katelyn Wheeler, David M Frazer, Donna Post Guillen, David W. Gandy, Janelle P. Wharry, Yu Lu

November 2022

Idaho National Laboratory
Idaho Falls, Idaho 83415

http://www.inl.gov

Prepared for the
U.S. Department of Energy
Under DOE Idaho Operations Office
Contract DE-AC07-05ID14517

Materials Science & Engineering A 857 (2022) 144058

Contents lists available at ScienceDirect

Materials Science & Engineering A

journal homepage: www.elsevier.com/locate/msea

Comparing structure-property evolution for PM-HIP and forged alloy 625 irradiated with neutrons to 1 dpa

Caleb Clement [a,*], Sowmya Panuganti [a], Patrick H. Warren [a], Yangyang Zhao [a], Yu Lu [b], Katelyn Wheeler [c], David Frazer [c], Donna P. Guillen [c], David W. Gandy [d], Janelle P. Wharry [a]

[a] School of Materials Engineering, Purdue University, West Lafayette, IN, USA
[b] Boise State University/ Center for Advanced Energy Studies, Idaho Falls, ID, USA
[c] Idaho National Laboratory, Idaho Falls, ID, USA
[d] Electric Power Research Institute, Charlotte, NC, USA

ARTICLE INFO

Keywords:
Powder metallurgy
Neutron irradiation
Tensile testing
Electron microscopy
Alloy 625
Ni alloy
Advanced manufacturing

ABSTRACT

The nuclear power industry has growing interest in qualifying powder metallurgy with hot isostatic pressing (PM-HIP) to replace traditional alloy fabrication methods for reactor structural components. But there is little known about the response of PM-HIP alloys to reactor conditions. This study directly compares the response of PM-HIP to forged Ni-base Alloy 625 under neutron irradiation doses ~0.5–1 displacements per atom (dpa) at temperatures ranging ~321–385 °C. Post-irradiation examination involves microstructure characterization, ASTM E8 uniaxial tensile testing, and fractography. Up through 1 dpa, PM-HIP Alloy 625 appears more resistant to irradiation-induced cavity nucleation than its forged counterpart, and consequently experiences significantly less hardening. This observed difference in performance can be explained by the higher initial dislocation density of the forged material, which represents an interstitial-biased sink that leaves a vacancy supersaturation to nucleate cavities. These findings show promise for qualification of PM-HIP Alloy 625 for nuclear applications, although higher dose studies are needed to assess the steady-state irradiated microstructure.

1. Introduction

Traditional manufacturing methods, such as casting and forging, have been used for structural components in the nuclear industry since its inception. However, with increasing demands of structural materials for Generation IV reactor systems [1–4], novel advanced manufacturing techniques such as powder metallurgy with hot isostatic pressing (PM-HIP) are receiving serious consideration for in-reactor use [5–7]. PM-HIP is a solid state manufacturing process wherein metal powders are densified into near-net shape components under high temperatures (~0.7T_m) and pressures (>100 MPa) [8,9]. PM-HIP materials offer numerous advantages over traditional forgings, including chemical homogeneity, fewer manufacturing defects, near-net shape production, and reduced reliance on machining and welding [5–7,10]. Additionally, HIP has also been used as a post-processing densification treatment for traditional and advanced manufactured materials [11,12]. Since PM-HIP fabricated 316L austenitic stainless steel has been approved by the ASME Boiler and Pressure Vessel Code (BPVC) for use in oil and gas energy production plants [6], there is growing interest in code-qualifying PM-HIP alloys for use in nuclear applications.

Efforts to systematically characterize irradiation effects and gather quantitative data on a number of PM-HIP structural alloys including austenitic steels, ferritic/martensitic steels, and Ni-based alloys are ongoing [13]. Previously, only limited investigations into the irradiation response of PM-HIP alloys had been performed. In studies by Carter et al. and Gasparrini et al. respectively, low-carbon steel SA508 was HIP processed then irradiated with neutrons (155 °C, 0.1 dpa) or He ions (room temperature, 0.6 dpa) [14,15]. Carter and coworkers observed irradiation hardening associated with uniform Ni–Mn–S–P clustering in both the bainite and ferrite phases, whereas Gasparrini and coworkers attributed considerable hardening to bubble/void formation. Finally, Jiang, et al. investigated void swelling in additively manufactured 316L stainless steel treated with HIP, under ion irradiation to 100 dpa at various temperatures [16]. They found that the HIP specimens display a longer incubation period before void swelling as compared to non-HIP counterparts [16]. These studies present inconclusive and widely differing findings on PM-HIP irradiation response; thus, further investigation is warranted.

* Corresponding author. 205 Gates Rd, West Lafayette, IN, 47906, USA.
E-mail address: clemen45@purdue.edu (C. Clement).

https://doi.org/10.1016/j.msea.2022.144058
Received 4 August 2022; Received in revised form 12 September 2022; Accepted 20 September 2022
Available online 28 September 2022

The present study focuses on Alloy 625, a Ni–Cr alloy solution-strengthened by Mo and Nb. Under long-term thermal aging, Alloy 625 can also be precipitation-strengthened by a fine homogenous dispersion of γ" phases [17,18]. Ni-based alloy grades including 625 have received renewed interest for nuclear core components, particularly in Generation IV reactor systems such as molten salt reactors [4,19,20]. In such systems, reactor core components will be subject to operating temperatures as high as 600–700 °C and irradiation fluences up to 10s–100s of dpa. Currently, the existing light water reactor fleet utilizes Alloy 625 in heat exchanger tubing, steam generators, pipes, and valves, due to its high temperature strength and resistance to corrosion [21–23]. One concern with Alloy 625 and other Ni-base alloys is the precipitation of hardening and embrittling phases such as the body-centered orthorhombic Pt_2Mo-type ordered phase. Such long-range ordering (LRO) is a diffusional process, and outside of irradiation conditions, the kinetics of Pt_2Mo-type precipitation are slow (10^5 h) [24]. However, under proton and neutron irradiation, radiation-enhanced diffusion increases the kinetics of precipitation by 2–3 orders of magnitude [25–28].

Progress has been made in systematically characterizing PM-HIP Alloy 625 for code qualification in nuclear applications. Guillen et al. first compared as-received wrought and PM-HIP Alloy 625 grain structures and mechanical properties utilizing far field high energy diffraction microscopy *in situ* tensile testing [29]. The study indicates that despite a finer grain structure, the PM-HIP Alloy 625 exhibits a lower yield strength than its wrought counterpart. Getto et al. compared the effects of thermal aging on grain structure and mechanical properties for wrought and PM-HIP Alloy 625 [7]. Through electron backscatter diffraction (EBSD) and nanoindentation, the study determines both fabrication methods exhibit unchanged hardness with thermal aging up to 800 °C, after which the wrought material experiences statistically significant softening. Most recently, Clement et al. investigated the dose and temperature dependencies of microstructure and mechanical properties of PM-HIP and forged Alloy 625 irradiated with 4.5 MeV Fe ions to 50 and 100 dpa at 400 °C and 500 °C [30]. That study found that the overall microstructural and mechanical responses between the PM-HIP and forged specimens are similar, but that a lower initial dislocation density in the PM-HIP leads to a more rapid evolution of the irradiation microstructure. However, emulation of neutron irradiation effects with ions is not sufficient for fully understanding how in-reactor conditions affect a structural alloy [28]. For example, ion irradiations cannot emulate cavity (i.e., voids and bubbles) nucleation that occurs in Ni-base alloys under neutron irradiation partially because the two-step transmutation reactions $^{58}Ni + n = {}^{59}Ni$ and $^{59}Ni + n = {}^{56}Fe + {}^{4}He$ only occur with neutrons as the irradiating specie [28,31,32]. Hence, neutron irradiation is necessary to truly capture in-reactor microstructural evolution, and to enable bulk mechanical testing [33].

The present study is the first to characterize the effects of neutron irradiation on the microstructural evolution and mechanical properties of Alloy 625 fabricated by PM-HIP as directly compared to a forged counterpart. In this work, TEM disks and threaded tensile bars are irradiated to a target dose of 1 dpa at a target temperature of approximately 400 °C. Mechanical properties are evaluated using ASME E8 tensile testing, while a combination of scanning transmission electron microscopy (S/TEM) and atom probe tomography (APT) are used to characterize the irradiated microstructure. Structure-property relationships under irradiation will be understood and interpreted in the context of the initial sink strength of the materials. The results of this study will contribute to the broader understanding of irradiation effects on Ni alloys, as well as the influence of fabrication method on irradiation response.

2. Materials and methods

2.1. Fabrication and irradiation

Ingots of forged and PM-HIP Alloy 625 are provided by the Electric Power Research Institute. The PM-HIP powder consolidation is conducted at 103 MPa and 1121 °C, followed by solution annealing at 1171 °C for 2 h with water quenching. The forged ingot is cast and hot rolled, then solution annealed at 1040 °C for 2 h 40 min with air cooling. The final two-step heat treatment consists of further solution annealing at 1075 °C for 30 min with water quenching, and thermal aging at 700 °C for 15 h with air cooling. Comprehensive details of the alloy fabrication processes are provided in Ref. [30], which shows that differences in fabrication and heat treatment history result in differences in as-received microstructures, and thus influence the irradiation response. Chemical composition, Table 1, is measured using inductively coupled plasma atomic emission spectroscopy for material certification and is confirmed using energy dispersive x-ray spectroscopy in a scanning electron microscope (SEM) [7,29].

Both the PM-HIP and forged ingots are machined into disc specimens and ASTM E8 standard threaded round tensile specimens. The discs are prepared by wire electrical discharge machining to 3 mm diameter and 150 μm thickness, then hand polished to mirror finish. The tensile specimens are computer numerical control machined to an overall length of 76.2 mm, gauge diameter of 6.35 mm, and surface roughness of 3.2 μm. Specimen drawings are shown in Fig. S1 in the supplementary information document. The specimens are loaded into capsule "400C/1 DPA (X)" for insertion into the Advanced Test Reactor (ATR) at Idaho National Laboratory (INL). The capsule is filled with a gas mixture of 80% helium and 20% argon and was irradiated in ATR inboard position A7 during cycle 164A. The target dose and temperature are 3.30×10^{20} n/cm^2, equivalent to 1 dpa, at 400 °C. Actual irradiation doses ranged 0.52–0.73 for the tensile bars and 1.05–1.06 dpa for the discs; and average temperatures ranged 321-354°C for the tensile bars and 385°C for the discs, Table 2. Comprehensive details of the neutron irradiation experiment design, fluence calculations, and temperature calculations, are provided in ref. [34].

After irradiation, the capsules are disassembled inside the hot cells at the Hot Fuel Examination Facility (HFEF) at the Materials and Fuels Complex at INL. Specimens are visually examined, then prepared for post-irradiation examination.The discs are decontaminated then electropolished in 12.5% perchloric acid +87.5% ethanol maintained at −17.5°C using a Struers Tenupol-5 operating at 18 V and a resultant current ~75 μA. The polished discs are then shipped to the Center for Advanced Energy Studies for microstructural characterization. The tensile bars are also decontaminated but remained in the HFEF hot cells for tensile testing.

2.2. Microstructural characterization

Prior to irradiation, the TEM disks are mechanically polished using SiC paper up to 1200 grit, then electropolished in 10% perchloric acid +90% methanol (by volume) solution at −40 °C and 35 V for 20 s. After irradiation, another electropolish is conducted using the identical solution and conditions to remove minor surface damage accumulated during handling, inspections, and decontamination. An FEI Quanta 3D dual-beam SEM/Focused Ion Beam (FIB) is used to create TEM lamellae from the TEM disks using the method described by Clement et al. [30]. A $2 \times 20 \times 3$ μm Pt deposition is placed across an area of interest spanning over a grain boundary. The area surrounding the deposition is then trenched out with the regular cross-section function at ± 1.5° stage tilt, before the lamellae are cut free and lifted out. The lamellae are then mounted onto Cu TEM half-grids, then thinned at ± 1.5° tilt using 30 kV Ga^+ ions at 1 nA current until achieving a 250 μm thickness. Then, a 5 kV polish at 0.26 nA and ±3.0° tilt is applied until electron transparency was achieved. A final 2 kV polish is applied at 47 pA and ±5.0° tilt for 3 min on each side to remove residual FIB surface damage and deposits. APT specimens are also fabricated using FIB milling as described in Refs. [35,36]. A lift-out lamella is sliced into ~1 μm pieces, each is then Pt welded to a Si post on a microtip array coupon. Iterative annular milling is used to shape each microtip into a needle with radius <100 nm. A

Table 1
Nominal chemical compositions (wt%) measured by ICP-AES (material certifications) and by SEM EDS; in all cases, the balance is Ni.

Alloy	Method	Fe	Cr	Mo	Nb	Mn	Si	Al	Ti	F	C	P	S	O
PM-HIP	ICP-AES	3.6	21.9	8.2	3.7	0.41	0.45	<0.05	0.006	–	0.01	0.003	0.003	–
	SEM EDS	3.57	23.0	7.25	3.75	0.544	0.688	0.106	–	0.22	–	–	–	0.25
Forged	ICP-AES	3.5	21.8	8.4	3.6	0.35	0.12	0.09	0.18	–	0.01	0.006	0.004	–
	SEM EDS	3.52	23.7	7.58	3.57	0.415	0.195	0.308	0.313	–	–	–	–	–

Table 2
Irradiation conditions for all specimens examined.

Specimen	Fluence [10^{20} n/cm^2]	Dose [dpa]	Maximum Temperature [°C]	Average Temperature [°C]
PM-HIP TEM Disc	3.47	1.05	386	385
PM-HIP Tensile Bar 1	2.38	0.73	352	339
PM-HIP Tensile Bar 2	1.76	0.53	330	321
Forged TEM Disc	3.51	1.06	386	385
Forged Tensile Bar 1	2.35	0.71	363	354
Forged Tensile Bar 2	1.74	0.52	346	335

low-energy 5 kV polish and 2 kV final cleaning are applied to minimize any damage associated with Ga^+ ion penetration from FIB milling.

An FEI (now a subsidiary of Thermo Fisher Scientific) Tecnai G2 F30 S/TEM is used for microstructural characterization of the irradiated samples. Dislocations and dislocation loops are analyzed using the down-zone bright field S/TEM technique first described by Parish et al. [37]. The samples are loaded in a double-tilt holder and tilted to the <101> zone axis. Then the microscope is placed in BF–S/TEM mode, which relaxes the g•b invisibility criterion and allows for simultaneous imaging of all loop types. This technique allows for faster characterization and strong contrast as compared to traditional weak beam dark field or rel-rod methods for dislocation and loop imaging [38,39]. Recent work by Xiu et al. [40] illustrates the orientation and contrast of faulted and perfect loops at each orientation in FCC materials using down-zone bright field S/TEM imaging. To image irradiation-induced voids, the Fresnel contrast through-focus technique is used in bright field TEM. Lamella thicknesses are calculated using the zero-loss peak in electron energy loss spectroscopy. S/TEM and TEM datasets are analyzed using Gatan Digital Micrograph and TEM Instrument Analysis software.

APT needles are analyzed in a Cameca Local Electrode Atom Probe 4000x HR instrument operating in laser pulse mode at 45 K base temperature. A pulse frequency and laser energy of 200 kHz and 60 pj, respectively are chosen. The Cameca IVAS Version 3.8.6 software is used to conduct 3D reconstructions of the needles. Reconstructions are rendered in IVAS using the procedure outlined in Ref. [41]. Five total needles from the irradiated forged material, and three total needles from the irradiated PM-HIP material, are run to >2 million ion histories and therefore had sufficient statistics for cluster analysis. Key cluster analysis variables N_{min} and d_{max}, the maximum separation distance and the minimum distance between atoms in a cluster, respectively, are found through an iterative process as described by Swenson and Wharry [41]. The average N_{min} value for the forged material is 17.75 ions, and for the PM-HIP material is 17.67 ions. The average d_{max} value for the forged material is 0.93 nm, and for the PM-HIP material is 1.41 nm. The number density, volume fraction, and radius of the precipitates, are subsequently calculated using the methods mentioned in Ref. [42].

2.3. Tensile testing

Uniaxial tensile testing is performed on the irradiated specimens as well as reference as-received specimens. Tests are conducted at room temperature in an inert argon environment using a 13 M Instron load frame inside the hot cells at the HFEF at INL. The test is conducted in accordance with ASTM E8 for threaded grip specimens. The crosshead speed is 0.279 mm/min which equates to a strain rate of 8.78×10^{-3} s^{-1}; after 10% strain, the speed is increased to 1.0 mm/min (0.0315 s^{-1}) until failure. A Lyra3 Tescan SEM at INL is then used to analyze the fracture surfaces of the PM-HIP and forged tensile bars.

3. Results

3.1. Summary of as-received microstructure

The as-received grain, precipitate, and dislocation microstructures from Refs. [7,29,30] are summarized in Table 3. From those studies, the PM-HIP and forged grain sizes are 6.9 ± 10 μm and 9.0 ± 8.2 μm respectively, and the initial PM-HIP and forged dislocation densities are $1.6 \pm 0.3 \times 10^{13}$ m^{-2} and $8.5 \pm 1.3 \times 10^{13}$ m^{-2} respectively. The lower dislocation density in the PM-HIP alloy is attributed to its higher processing temperature and the absence of rolling or other deformation processing. Both fabrication methods exhibit micro-scale (Nb,Mo)-rich carbides preferentially decorating the grain boundaries. Residual oxides from powder processing are also observed in the PM-HIP material. The γ'' precipitation strengthening phase is not observed in either the PM-HIP or forged materials, which is reasonable given the heat treatments employed. Amongst these microstructural features, the dislocation density has the greatest influence on the initial sink strength of the alloys. From Table 3, the calculated sink strength values are 0.2×10^{14} m^{-2} and 1.22×10^{14} m^{-2} for the PM-HIP and forged specimens respectively.

3.2. Irradiation-induced loops & cavities

After neutron irradiation, a homogenous distribution of dislocation loops and cavities are observed in both specimens. Representative micrographs of these features can be seen in Fig. 1, with quantifications provided in Table 3. The dislocation loop sizes and number densities differ, with PM-HIP having smaller (~5 nm vs. ~8 nm), but more numerous (~1.4 vs. ~1.1×10^{20} m^{-3}) loops than its forged counterpart. This follows the trend observed in PM-HIP and forged alloy 625 irradiated by Fe^+ ions [30], although the loop sizes and number densities in the present study are lower than those generated by Fe^+ ion irradiation to higher doses (50 and 100 dpa) at higher temperatures (400°C and 500°C) in Ref. [30]. This is reasonable, given that dislocation loops in Ni-based and other fcc alloys tend to grow in both diameter and density in the low dose regimes (such as the doses in the current study) before plateauing at doses >10 dpa [28,43].

Both the PM-HIP and forged specimens have cavity sizes ~2 nm, which are too small to distinguish voids (faceted) from bubbles, so this paper will henceforth describe cavities as inclusive of features that are potentially voids and bubbles. While cavity sizes are identical between the PM-HIP and forged materials, the cavity number density in the forged material (~37.6×10^{20} m^{-3}) exceeds that of the PM-HIP by a factor of >4 (8.96×10^{20} m^{-3}). Notably, cavities are not observed in the

Table 3
Summary of quantitative microstructure evolution, with accompanying calculations for initial sink strength and predicted irradiation hardening.

Specimen	Feature	Measurement	As-Received (from Ref. [30])		Irradiated (~1 dpa)	
			Value	Sink Strength [10^{14} m^{-2}]	Value	Expected hardening [MPa]
PM-HIP	Grains	Diameter [10^{-6} m]	6.9 ± 10	0.005	n/a	n/a
	Loops	Diameter [10^{-9} m]	–		4.8 ± 0.21	15.2 ± 0.2
		No. density [10^{20} m^{-2}]	–	–	1.41 ± 0.04	
	Cavities	Diameter [10^{-9}m]	–	–	2.4 ± 0.20	90.3 ± 5.1
		No. density [$10^{20}m^{-3}$]	–	–	8.96 ± 3.15	
	Si clusters	Diameter [10^{-9} m]	–	–	5.77 ± 0.19	36.3 ± 3.3
		No. density [10^{22} m^{-2}]	–	–	6.69 ± 1.68	
	Lines	Density [10^{13} m^{-2}]	1.6 ± 0.3	0.2	1.37 ± 0.26	-14.0 ± 3.9
	Total	–	–	–	–	128 ± 13
Forged	Grains	Diameter [10^{-6} m]	9.0 ± 8.2	0.003	n/a	n/a
	Loops	Diameter [x10^{-9} m]	–	–	8.1 ± 0.24	29.1 ± 0.5
		No. density [x10^{20} m^{-2}]	–	–	1.10 ± 0.02	
	Cavities	Diameter [x10^{-9}m]	–	–	2.2 ± 0.12	172 ± 2.8
		No. density [x$10^{20}m^{-3}$]	–	–	37.6 ± 15.4	
	Si clusters	Diameter [x10^{-9} m]	–	–	3.56 ± 0.27	24.8 ± 3.0
		No. density [x10^{22} m^{-2}]	–	–	4.97 ± 0.95	
	Lines	Density [x10^{13} m^{-2}]	8.5 ± 1.3	1.22	6.28 ± 1.68	-43.5 ± 3.8
	Total	–	–	–	–	182 ± 10

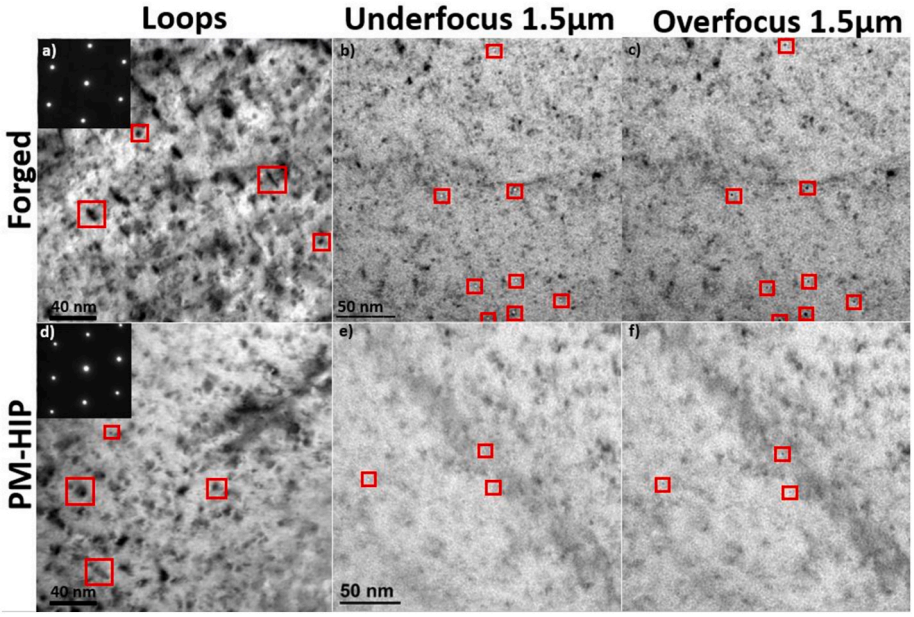

Fig. 1. Representative micrographs of irradiation-induced loops and cavities in (a–c) forged and (d–f) PM-HIP Alloy 625. Loops are imaged using down-zone BF–S/TEM, and example loops are boxed. Cavities are imaged using through-focus imaging, with both under- and over-focused images shown, with example cavities boxed.

identical PM-HIP and forged materials under Fe^{2+} ion irradiation [30]. But this is reasonable considering the temperature shift theory [44], which suggests that the higher ion irradiation dose rate requires higher temperatures for defect migration to have comparable kinetics to neutron irradiation. Additionally, Getto et al. show that in ferritic/martensitic steel, cavity formation is unlikely by ion irradiation alone at doses <100 dpa without concurrent He injection [45].

The cavity density observed in the current study is larger than that reported in a study of 2 MeV proton irradiated Alloy 625 by Tucker et al. [27]. Specifically, they observe a number density of 1.4×10^{20} m^{-3} at a similar dose as the current study (1.5 dpa) but lower temperature (300 °C). This can be reconciled because beginning at around 400 °C, fcc alloys enter the Stage III temperature regime, where the kinetics of vacancy migration increase such that cavity nucleation occurs at significantly greater densities [28,43]. Coupled with the higher dose rate of proton irradiation reducing the effective vacancy migration, the higher cavity number densities in the current study are reasonable.

Both the PM-HIP and forged specimens experience a decrease in network dislocation density during irradiation to 1 dpa. This behavior is in agreement with the Garner and Wolfer model of the evolution of network dislocation density in irradiated metals [46], wherein the initial dislocation density in AISI 316 steel decreases during neutron irradiation through 25 dpa. Note, however, that this decrease may not be entirely due to irradiation, but may partly be attributed to thermal annealing over the long duration of the material being held at an elevated temperature. Chen et al. additionally observes a decrease in dislocation density for Hastelloy N irradiated with room temperature Xe^{20+} ions, which they ascribed to dislocation climb to free surfaces by the absorption of interstitials under irradiation [47]. In the current work, the irradiation temperature, time, and dose may provide sufficient thermal energy and interstitial population to activate migration and climb of network dislocations to free surfaces [46,47]. At the same time, the dose in the current study is not sufficient for the faulted loops to grow, interact with the network, then unfault, which would otherwise enable the total dislocation density to achieve a steady-state. Work compiled by Zinkle indicates that fcc alloys irradiated over 375–400 °C

do not reach a steady-state loop density until doses >10 dpa [43].

3.3. Irradiation-induced precipitation & clustering

Selected area electron diffraction patterns along the [001] zone axis seen in Fig. 2 show no superlattice spots indicative of precipitation. While irradiation-induced LRO Pt_2Mo-type precipitates can nucleate in Alloy 625 over irradiation temperatures ranging 300-360°C, their formation is sensitive to the initial heat treatment (both time and temperature) of the alloy [25–27,48]. For example, Bajaj et al. observe neutron irradiation-induced Pt_2Mo-type precipitates after 2.4×10^{20} n/cm^2 (~0.7 dpa) at 360 °C in Alloy 625 initially aged at 663 °C for 80 h [26], whereas in the current study, the forged material is aged for only 15 h. Song et al. use a higher temperature heat treatment of 955 °C for only 0.5 h, and observe Pt_2Mo-type precipitates after 2 MeV proton irradiation to 2.5 dpa at 360 °C [48]. Higher irradiation doses may be necessary to induce precipitation in less-aged or un-aged materials. For Alloy 625 aged at 650 °C for 25 h, Yu and Marquis report a dose of 5 dpa is necessary for 2 MeV proton irradiation at 300 °C to induce Pt_2Mo-type precipitation; meanwhile, their solution annealed but un-aged Alloy 625 does not display irradiation-induced precipitation until 11 dpa [25].

APT identifies Si clustering in both the PM-HIP and forged specimens. While the number density of clusters is comparable between the two fabrication methods, the cluster diameter and volume fraction are greater in the PM-HIP than in the forged. Representative APT needle reconstructions can be seen in Fig. 3, while quantitative data of the Si clusters (averaged over all needles examined) can be seen in Fig. 5. Formation of Si clustering after irradiation has previously been observed in proton irradiated Alloy 625 and Alloy 625+ [22,25,27,49], as a likely precursor to the formation of $L1_2$-structured Ni_3Si precipitates [49].

The larger Si clusters in the PM-HIP material than in the forging may either be due to the higher bulk Si concentration in PM-HIP (Table 1) or due to loss of Si to radiation induced segregation (RIS) at dislocation loops and networks in the forged specimen (see Fig. S2 in the supplementary information document). The phenomenon of Si segregation to dislocation features has been previously reported in proton irradiated Alloy 625 and Alloy 625+ [25,49], but in the current study occurs only in the forged material. However, the smaller average loop size in the PM-HIP material could render Si RIS to be unresolvable as loops, and instead interpreted merely as clusters. Additionally, the lower dislocation line density in the PM-HIP material reduces the likelihood of capturing a dislocation within the APT needle volume. RIS of Si occurs when irradiation generates a vacancy supersaturation, which results in a driving vacancy flux that drags substitutional Si atoms towards dislocation cores due to positive Si-vacancy coupling [50].

3.4. Tensile testing

Engineering stress-strain curves from uniaxial tensile testing are shown in Fig. 3(a). The corresponding values of yield strength (σ_Y) at 0.2% strain offset, ultimate tensile strength (UTS), Young's modulus, and elongation at failure are quantified in Table 4. The tensile testing results will be presented systematically, with the as-received tensile data reported first, followed by an examination of the irradiated tensile data as a function of irradiation dose with fracture surfaces presented for the lowest dose specimens from each material.

The as-received PM-HIP and forged specimens generally exhibit similar initial mechanical properties. They have virtually identical σ_Y (~460 MPa) and similar UTS (768 MPa and 862 MPa, respectively), which are in close agreement with values from the archival literature [29,51] and the ASME Boiler and Pressure Vessel Code (BPVC) for Alloy 625 [52]. The Young's modulus values are 193 GPa and 217 GPa for the as-received PM-HIP and forged specimens respectively, which are higher than measured from dogbone shaped miniature tensile specimens cut from the identical PM-HIP and forged ingots reported in Ref. [29]. However, the higher moduli in the present study may be attributed to sub-sized mechanical testing specimens tending to exhibit lower elastic moduli than standardized specimens [53]. The as-received PM-HIP specimen fractures prematurely, resulting in artificially suppressed elongation at failure. Meanwhile, elongation of the forged specimen (56.0%) is in close agreement with values reported for Alloy 625 in the archival literature [54,55].

Under irradiation, the PM-HIP material begins to exhibit superior mechanical performance compared to the forged material. At ~0.5 dpa, the PM-HIP specimen exhibits less than half the irradiation-induced increase in σ_Y (66.8 MPa) as the forged specimen (146 MPa); this difference is exacerbated at ~0.7 dpa (84.7 MPa increase in PM-HIP, 239 MPa increase in forged). The irradiated PM-HIP specimens also exhibit greater ductility (total elongation of 45.9% and 39.2% at ~0.5 and ~0.7 dpa, respectively) than the forged specimens (total elongation 40.4% and 36.0% at the respective doses). These findings suggest the PM-HIP material is more resistant to irradiation-induced hardening and embrittlement. Accordingly, the ~0.5 dpa fracture surface images, Fig. 4 (b–e), reveal pronounced ductile cup-cone fracture in the PM-HIP specimen, while the forged specimen displays shearing. However, the surface dimples are larger on the forged specimen than on the PM-HIP specimen, suggesting that the forged specimen nevertheless fractures in a ductile manner. These results are notably different from a previous direct comparison of mechanical behavior of irradiated PM-HIP to forged material from Lind and Bergenlid [56,57], who report greater irradiation-induced ductility reduction in PM-HIP than in forged 316L austenitic stainless steel.

Trends in UTS and Young's modulus are less clear in the irradiated PM-HIP and forged materials, Table 4. The PM-HIP and forged specimens have similar UTS at a given dose. But at ~0.5 dpa, the UTS is higher for the PM-HIP than for forged, while this trend reverses at ~0.7 dpa. Young's modulus appears to decrease with irradiation. Before irradiation, the PM-HIP material has higher modulus than the forged, but the opposite is true at ~0.5 and ~0.7 dpa. An irradiation-induced reduction in Young's modulus is known to occur in Alloy 625 [58]. The decrease in Young's modulus is correlated to increasing irradiation-induced void volume [59].

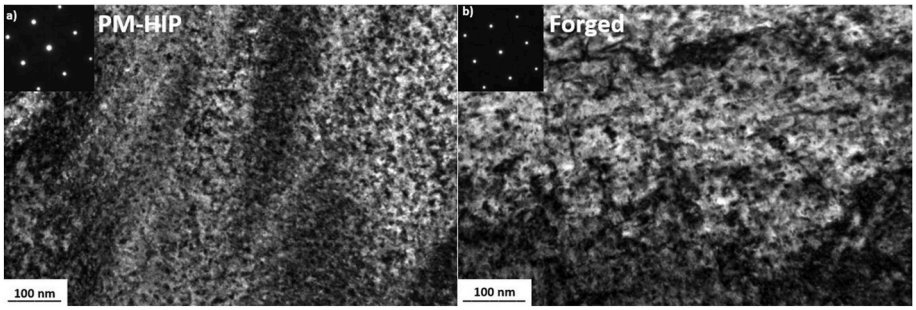

Fig. 2. TEM bright field images along [001] zone axis in (a) PM-HIP and (b) forged specimens, with inset diffraction patterns showing LRO after irradiation.

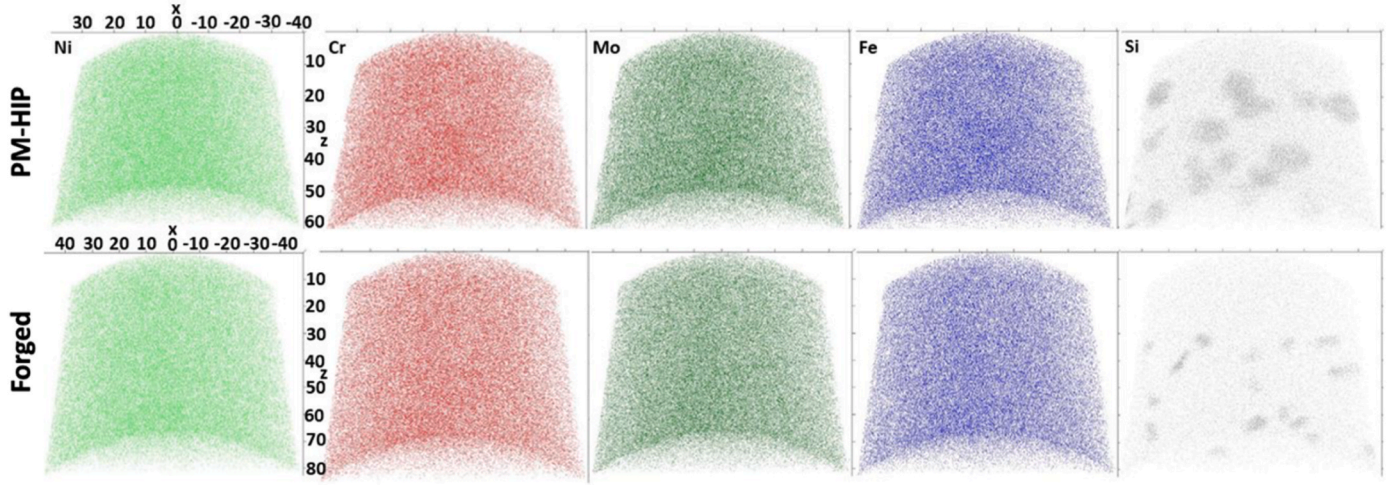

Fig. 3. Representative APT tip 3D reconstructions from irradiated a) PM-HIP and b) Forged Alloy 625, showing no clustering or segregation of major alloying species Ni, Cr, Mo, or Fe, but the presence of Si nanoclustering.

Table 4
Summary of mechanical properties from uniaxial tensile testing (* indicates premature fracture).

Alloy	Dose [dpa]	σ_y [MPa]	$\Delta\sigma_y$ [MPa]	Modulus [GPa]	UTS [MPa]	Elongation at failure [%]
PM-HIP	0	462.2	–	193	768	13.7*
	0.53	529.0	66.8	179	1004	45.9
	0.73	546.9	84.7	89	1011	39.2
Forged	0	455.8	–	217	862	56.0
	0.52	602.2	146	94	964	40.4
	0.71	694.4	239	73	1088	36.0

4. Discussion

4.1. Structure-property relationships

The irradiated microstructure is used to calculate the expected irradiation hardening (i.e., $\Delta\sigma_y$) shown in Table 3 using the Orowan dispersed barrier hardening (DBH) model:

$$\Delta\sigma_{yi} = \alpha_i M \mu b \sqrt{N_i d_i}$$

with α being the strength factor of a particular obstacle [60–62], M being the Taylor factor of 3.06 for fcc materials [63], μ being the shear modulus which is 81.4 GPa for Alloy 625 [51], b being the Burgers vector of 0.247 nm [64], and i being the type of obstacle. Here, four obstacle types are considered in the DBH model: dislocation loops, dislocation lines, cavities, and clusters. Cavities have the highest α at 1.0, while dislocation loops are divided by size with small loops and large loops having α values of 0.3 and 0.5, respectively. This bifurcation of loop strength factors is predicated on work by Tan and Busby [61] as well as Lucas [60] detailing size dependence of defects on their overall contribution to hardening. The strength factors for all obstacles can be seen in Table S1 in the supplementary information document. Because the microstructure specimens and the tensile specimens have different total fluences (recall Table 2), the DBH model will be used to explain the probable contributions of various defects to the overall irradiation hardening.

From Table 3 and Fig. 5, cavities are the most significant contributor to the observed irradiation hardening, and the difference in cavity density also is the most significant contributor to the difference in hardening observed between the PM-HIP and forged specimens. The DBH calculation predicts greater hardening in the forged than the PM-HIP, which is in good agreement with the experimental hardening trends at both ~0.5 dpa as well as ~0.7 dpa. Although the nucleation and growth of dislocation loops and clusters contribute to hardening and a reduction in ductility in both materials, the excess cavities in the forged specimens appear to be the major contributor to the differences in hardening and total elongation. These cavities are favored by the high initial dislocation density and sink strength of the forged material, which

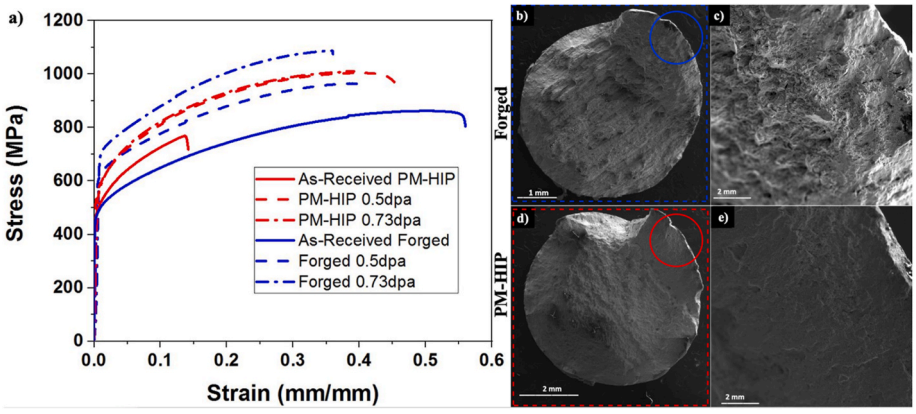

Fig. 4. (a) Uniaxial tensile stress-strain curves from as-received, ~0.5 dpa, and ~0.7 dpa PM-HIP and forged Alloy 625; fracture surfaces from ~0.5 dpa (b) forged and (d) PM-HIP tensile specimens, with circled regions shown in higher magnification in (c) and (e) respectively.

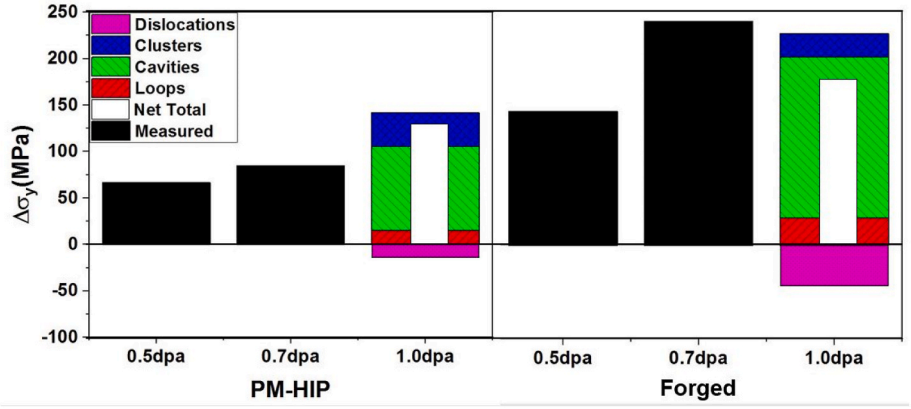

Fig. 5. Comparison of (a) PM-HIP to (b) forged irradiation hardening, measured as a function of dose at ~0.5–0.7 dpa, and to dispersed barrier hardening calculation at 1 dpa.

will be the focus of Section 4.2.

4.2. Sink strength effects

The initial sink strength directly controls the rate at which the microstructure evolves under irradiation [30]. In the present study, the initial sink strength of the as-received forged material is higher than that of the PM-HIP material by a factor of ~6, due to the dominant influence of the dislocation network density on the total sink strength (Table 3). Since dislocations are a biased preferential sink for interstitials [65–67], a supersaturation of vacancies will remain in the microstructure, which over time coalesce and combine with transmutation helium into cavities [28,68–71]. Thus, the higher as-received dislocation density explains the higher number density of cavities in the irradiated forged material. Moreover, since cavities are the microstructural features with the greatest influence on irradiation hardening, the initial dislocation density and sink strength can also explain the higher hardening in the forged specimens. Additionally, cavities may migrate in reactor conditions under the presence of an applied tensile stress to grain boundaries, which leads to further embrittlement, loss of ductility, and a transition from transgranular to intergranular fracture leading to brittle failure below prescribed mechanical conditions in austenitic alloys [28,32,72,73].

These results underscore the importance of sink bias in predicting the irradiation resistance of materials. Although engineering irradiation tolerance by introducing sinks has been the subject of extensive research over the past ~ decade [74–78], much of these efforts have focused on engineered interfaces or grain boundaries, which are generally understood to be unbiased or variably biased depending on defect pre-loading [79,80]. Consequently, higher unbiased sink strengths enhance resistance to irradiation defect accumulation, and thus reduce irradiation hardening, e.g. in oxide dispersion strengthened steels [81,82]. Similarly, lower unbiased sink strengths have been associated with irradiation softening [83]. The relationship between increasing unbiased sink strength and reducing hardening is opposite that observed in the present study, wherein a reduced biased sink strength also suppresses irradiation hardening.

The dose evolution of irradiation hardening may also be explained by the initial sink strength. The uniaxial tensile irradiation hardening of the forged material increases by nearly 100 MPa between ~0.5 and ~0.7 dpa, while the irradiation hardening in the PM-HIP material remains relatively unchanged over the same dose range. In the forged material, cavities contribute nearly 95% of the irradiation hardening. Cavity formation requires that interstitials first diffuse to biased sinks (i.e., network dislocations) before vacancies nucleate into cavities. But because interstitials are faster diffusers than vacancies, cavity nucleation – and thus hardening – in the forged material may onset at a relatively higher dose. On the other hand, in the PM-HIP material, cavities contribute only 70% of the total irradiation hardening. The lower initial sink strength enables both interstitials and vacancies to contribute to microstructure evolution, and thus the irradiation hardening may onset at a relatively lower dose in the PM-HIP material. Hence, the PM-HIP microstructure likely develops more rapidly (i.e. at lower dose) than that of the forged, enabling the PM-HIP to reach mechanical stasis before the forged counterpart. Of course, these findings are based on a total neutron irradiation damage dose of 1 dpa, at which point the material is not expected to have yet reached steady-state point defect concentration [28,43]. However, the conclusions that can be drawn remain relevant for informing the initial response of PM-HIP and forged Alloy 625 in the low-dose transient regime, which ultimately impacts the dose at which steady-state is attained.

Overall, the PM-HIP Alloy 625 responds to neutron irradiation favorably as compared to its forged counterpart. This can be attributed in part to a lower initial dislocation sink strength, which creates starting conditions less favorable for cavity nucleation and hardening. Compositional differences between the PM-HIP and forged specimens are noted and are believed to have minor effects such as larger irradiation-induced Si clusters in the PM-HIP specimen. However, differences in network dislocation density inherent to the PM-HIP and forged materials are most influential over their irradiation behavior because of the biased sink strength. Tailoring fabrication conditions to engineer sink bias and thus enhance irradiation tolerance presents an opportunity for deploying alloys fabricated by PM-HIP or other advanced processing methods in nuclear applications.

5. Conclusion

PM-HIP and forged Alloy 625 are irradiated in the Advanced Test Reactor with thermal neutrons. Microstructure characterization specimens are irradiated to doses of 1.05–1.06 dpa at an average temperature of 385 °C; uniaxial tensile specimens are irradiated to doses of 0.52–0.53 dpa and 0.71–0.73 dpa at average temperatures ranging 321-354°C. The irradiation-induced microstructural evolution and change in mechanical properties are directly compared across fabrication types. Major conclusions are:

- At least through doses of ~1 dpa, PM-HIP Alloy 625 appears more resistant to irradiation-induced cavity nucleation than its forged counterpart, and thus exhibits less irradiation hardening. This is attributed to the higher initial dislocation density in the forged specimen, which are biased sinks for interstitials.
- The PM-HIP specimen has larger Si nanoclusters than the forged, while the forged has larger dislocation loops than the PM-HIP; these

differences essentially offset one another in their influence on irradiation hardening between the two materials.

- Between ~0.5 and ~0.7 dpa, irradiation hardening appears to saturate in the PM-HIP tensile specimens but does not saturate in the forged tensile specimens. This may be explained by differences in initial biased sink density between the PM-HIP and forged materials.
- PM-HIP specimens exhibit greater ductility as a result of irradiation than forged specimens.
- The comparative irradiation performance of PM-HIP Alloy 625 over its forged counterpart supports the qualification of PM-HIP components for nuclear applications up to the ~1 dpa damage dose studied. Higher dose studies may be necessary to inform steady-state irradiation response.

CRediT authorship contribution statement

Caleb Clement: Investigation, Formal analysis, Writing – original draft, Writing – review & editing. **Sowmya Panuganti:** Investigation, Formal analysis, Writing – original draft. **Patrick H. Warren:** Investigation, Data curation. **Yangyang Zhao:** Investigation, Data curation. **Yu Lu:** Data curation. **Katelyn Wheeler:** Investigation, Data curation. **David Frazer:** Data curation. **Donna P. Guillen:** Conceptualization, Formal analysis, Funding acquisition. **David W. Gandy:** Project administration, Conceptualization. **Janelle P. Wharry:** Conceptualization, Funding acquisition, Writing – review & editing.

Declaration of competing interest

The authors declare that they have no known competing financial interests or personal relationships that could have appeared to influence the work reported in this paper.

Data availability

Data will be made available on request.

Acknowledgements

The authors thank Dr. Yaqiao Wu, Jeremy Burgener, Megha Dubey, and the staff at the Center for Advanced Energy Studies (CAES) for their assistance with microscopy and specimen handling. Additionally, the authors thank the irradiation experiment manager Katie Anderson, post-irradiation experiment manager Collin Knight, and the staff at the ATR and HFEF at Idaho National Laboratory for their assistance with ATR irradiation and post-irradiation examination. This work was supported by the Electric Power Research Institute (EPRI). CC was partially supported by the US Nuclear Regulatory Commission through Grant 31310021M0035. Irradiation experiments and post-irradiation examination were supported by the U.S. Department of Energy – Office of Nuclear Energy, through the Nuclear Science User Facilities (NSUF) contract 15–8242.

Appendix A. Supplementary data

Supplementary data to this article can be found online at https://doi.org/10.1016/j.msea.2022.144058.

References

[1] X. Lou, D. Gandy, Advanced manufacturing for nuclear energy, JOM (J. Occup. Med.) 71 (2019) 2834–2836, https://doi.org/10.1007/s11837-019-03607-4.
[2] P. Yvon, F. Carré, Structural materials challenges for advanced reactor systems, J. Nucl. Mater. 385 (2009) 217–222, https://doi.org/10.1016/j.jnucmat.2008.11.026.
[3] K.L. Murty, I. Charit, Structural materials for Gen-IV nuclear reactors: challenges and opportunities, J. Nucl. Mater. 383 (2008) 189–195, https://doi.org/10.1016/j.jnucmat.2008.08.044.
[4] P.P. Joshi, N. Kumar, K.L. Murty, Materials for Nuclear Reactors, Elsevier Ltd., 2020, https://doi.org/10.1016/b978-0-12-803581-8.12070-3.
[5] D.W. Gandy, J. Shingledecker, J. Siefert, Overcoming Barriers for Using PM/HIP Technology to Manufacture Large Power Generation Components PM/HIP opens up a new method of manufacturing high pressure-retaining components for use in the power-generation industry. (a) (b), Adv. Mater. Process. 1 (2012) 19–23.
[6] D.W. Gandy, PM-HIP Research for Structural and Pressuring Retaining Applications within the Electric Power Industry, 2015.
[7] E. Getto, B. Tobie, E. Bautista, A.L. Bullens, Z.T. Kroll, M.J. Pavel, K.S. Mao, D. W. Gandy, J.P. Wharry, Thermal aging and the Hall–petch relationship of PM-HIP and wrought alloy 625, JOM (J. Occup. Med.) 71 (2019) 2837–2845, https://doi.org/10.1007/s11837-019-03532-6.
[8] H. V Atkinson, S. Davies, Fundamental aspects of hot isostatic pressing: an overview, Metall. Mater. Trans. 31A (2000). https://link.springer.com/content/pdf/10.1007%2Fs11661-000-0078-2.pdf. (Accessed 26 August 2019). accessed.
[9] European Powder Metallurgy Association, Introduction to PM HIP technology, n.d. http://www.epma.com/pdfs/Final_HIP_Brochure_Low_res.pdf.
[10] H.R. Dugdale, J.B. Borradaile, Development of hot isostatically pressed nickel based alloys for nuclear applications, Energy Mater. Mater. Sci. Eng. Energy Syst. 8 (2013) 374–381, https://doi.org/10.1179/1743290113Y.0000000076.
[11] M.H. Bocanegra-Bernal, Review Hot Isostatic Pressing (HIP) Technology and its Applications to Metals and Ceramics, n.d.
[12] A. Kreitcberg, V. Brailovski, S. Turenne, Effect of heat treatment and hot isostatic pressing on the microstructure and mechanical properties of Inconel 625 alloy processed by laser powder bed fusion, Mater. Sci. Eng. 689 (2017) 1–10, https://doi.org/10.1016/j.msea.2017.02.038.
[13] D.P. Guillen, J.P. Wharry, D.W. Gandy, Ongoing irradiations of nuclear structural materials fabricated by powder metallurgy with hot isostatic pressing, Trans. Am. Nucl. Soc. 116 (2017) 392–393.
[14] M. Carter, C. Gasparrini, J.O. Douglas, N. Riddle, L. Edwards, P.A.J. Bagot, C. D. Hardie, M.R. Wenman, M.P. Moody, On the influence of microstructure on the neutron irradiation response of HIPed SA508 steel for nuclear applications, J. Nucl. Mater. 559 (2022), 153435, https://doi.org/10.1016/j.jnucmat.2021.153435.
[15] C. Gasparrini, A. Xu, K. Short, T. Wei, J. Davis, T. Palmer, D. Bhattacharyya, L. Edwards, M.R. Wenman, Micromechanical testing of unirradiated and helium ion irradiated SA508 reactor pressure vessel steels: nanoindentation vs in-situ microtensile testing, Mater. Sci. Eng. 796 (2020), https://doi.org/10.1016/j.msea.2020.139942.
[16] L. Jiang, M. Song, L. Yang, J. Yang, D. Du, X. Lou, Y. Chen, A comparison study of void swelling in additively manufactured and cold-worked 316L stainless steels under ion irradiation, J. Nucl. Mater. 551 (2021), 152946, https://doi.org/10.1016/j.jnucmat.2021.152946.
[17] S.K. Rai, A. Kumar, V. Shankar, T. Jayakumar, K.B.S. Rao, B. Raj, Characterization of microstructures in Inconel 625 using X-ray diffraction peak broadening and lattice parameter measurements, Scripta Mater. 51 (2004) 59–63, https://doi.org/10.1016/j.scriptamat.2004.03.017.
[18] L.J. Yu, E.A. Marquis, Precipitation behavior of alloy 625 and alloy 625 plus, J. Alloys Compd. 811 (2019), 151916, https://doi.org/10.1016/j.jallcom.2019.151916.
[19] A.F. Rowcliffe, L.K. Mansur, D.T. Hoelzer, R.K. Nanstad, Perspectives on radiation effects in nickel-base alloys for applications in advanced reactors, J. Nucl. Mater. 392 (2009) 341–352, https://doi.org/10.1016/j.jnucmat.2009.03.023.
[20] J. Tucker, A. Hahn, Modeling and Validation of Irradiation Damage in Ni-Based Alloys for Long-Term LWR Applications Reactor Concepts Research Development and Demonstration, (n.d).
[21] G.S. Was, M. Song, M. Wang, IASCC Susceptibility and Evolution of Microstructure in Several Ni-Base Alloys after Proton Irradiation, 2015.
[22] M. Song, C.R. Lear, C.M. Parish, M. Wang, G.S. Was, Radiation tolerance of commercial and advanced alloys for core internals: a comprehensive microstructural characterization, J. Nucl. Mater. 510 (2018) 396–413, https://doi.org/10.1016/j.jnucmat.2018.08.035.
[23] M. Wang, M. Song, C.R. Lear, G.S. Was, Irradiation assisted stress corrosion cracking of commercial and advanced alloys for light water reactor core internals, J. Nucl. Mater. 515 (2019) 52–70, https://doi.org/10.1016/j.jnucmat.2018.12.015.
[24] M. Sundararaman, L. Kumar, G. Eswara Prasad, P. Mukhopadhyay, S. Banerjee, Precipitation of an intermetallic phase with Pt2Mo-type structure in alloy 625, Metall. Mater. Trans. A Phys. Metall. Mater. Sci. 30 (1999) 41–52, https://doi.org/10.1007/s11661-999-0194-6.
[25] L. Yu, E.A. Marquis, Microstructural responses of alloy 625 and alloy 625 plus under ion and proton irradiations, JOM (J. Occup. Med.) (2020), https://doi.org/10.1007/s11837-020-04211-7.
[26] R. Bajaj, W.J. Mills, M.R. Lebo, B.Z. Hyatt, M.G. Burke, Irradiation-Assisted stress corrosion cracking of HTH alloy X-750 and alloy 625, in: Int. Symp. Environ. Degrad. Mater. Nucl. Power Plants, Water React., 1995.
[27] J. Tucker, Modeling and Validation of Irradiation Damage in Ni-Based Alloys for Long-Term LWR Applications, 2019.
[28] G.S. Was, G.S. Was, Fundamentals of Radiation Materials Science, 2017, https://doi.org/10.1007/978-1-4939-3438-6_1.
[29] D.P. Guillen, D.C. Pagan, E.M. Getto, J.P. Wharry, In situ tensile study of PM-HIP and wrought 316 L stainless steel and Inconel 625 alloys with high energy diffraction microscopy, Mater. Sci. Eng. 738 (2018) 380–388, https://doi.org/10.1016/j.msea.2018.09.083.
[30] C. Clement, Y. Zhao, P. Warren, X. Liu, S. Xue, D.W. Gandy, J.P. Wharry, Comparison of ion irradiation effects in PM-HIP and forged alloy 625, J. Nucl. Mater. 558 (2021), 153390, https://doi.org/10.1016/j.jnucmat.2021.153390.

[31] L. Luneville, J.C. Sublet, D. Simeone, Impact of nuclear transmutations on the primary damage production: the example of Ni based steels, J. Nucl. Mater. 505 (2018) 262–266, https://doi.org/10.1016/j.jnucmat.2017.06.039.

[32] M. Griffiths, R. Boothby, Radiation Effects in Nickel-Based Alloys, 2020, https://doi.org/10.1016/b978-0-12-803581-8.11705-9.

[33] J.P. Wharry, K.H. Yano, P.V. Patki, Intrinsic-extrinsic size effect relationship for micromechanical tests, Scripta Mater. 162 (2019) 63–67, https://doi.org/10.1016/j.scriptamat.2018.10.045.

[34] D.P. Guillen, J.P. Wharry, G. Housley, C.D. Hale, J. Brookman, D.W. Gandy, Irradiation experiment design for the evaluation of PM-HIP alloys for nuclear reactors, 2022. Submitted for publication.

[35] A. Sen, M. Bachhav, F. Vurpillot, J.M. Mann, P.K. Morgan, T.A. Prusnick, J. P. Wharry, Influence of field conditions on quantitative analysis of single crystal thorium dioxide by atom probe tomography, Ultramicroscopy 220 (2021), 113167, https://doi.org/10.1016/j.ultramic.2020.113167.

[36] M.K. Miller, K.F. Russell, K. Thompson, R. Alvis, D.J. Larson, Review of atom probe FIB-based specimen preparation methods, Microsc. Microanal. 13 (2007) 428–436, https://doi.org/10.1017/S1431927607070845.

[37] C.M. Parish, K.G. Field, A.G. Certain, J.P. Wharry, Application of STEM characterization for investigating radiation effects in BCC Fe-based alloys, J. Mater. Res. 30 (2015) 1275–1289, https://doi.org/10.1557/jmr.2015.32.

[38] P. Xiu, Y.N. Osetsky, L. Jiang, G. Velisa, Y. Tong, H. Bei, W.J. Weber, Y. Zhang, L. Wang, Dislocation loop evolution and radiation hardening in nickel-based concentrated solid solution alloys, J. Nucl. Mater. 538 (2020), 152247, https://doi.org/10.1016/j.jnucmat.2020.152247.

[39] K.G. Field, S.A. Briggs, K. Sridharan, Y. Yamamoto, R.H. Howard, Dislocation loop formation in model FeCrAl alloys after neutron irradiation below 1 dpa, J. Nucl. Mater. 495 (2017) 20–26, https://doi.org/10.1016/j.jnucmat.2017.07.061.

[40] P. Xiu, H. Bei, Y. Zhang, L. Wang, K.G. Field, STEM characterization of dislocation loops in irradiated FCC alloys, J. Nucl. Mater. 544 (2021), 152658, https://doi.org/10.1016/j.jnucmat.2020.152658.

[41] M.J. Swenson, J.P. Wharry, The comparison of microstructure and nanocluster evolution in proton and neutron irradiated Fe-9%Cr ODS steel to 3 dpa at 500 °c, J. Nucl. Mater. 467 (2015) 97–112, https://doi.org/10.1016/j.jnucmat.2015.09.022.

[42] M. Bachhav, G. Robert Odette, E.A. Marquis, α′ precipitation in neutron-irradiated Fe-Cr alloys, Scripta Mater. 74 (2014) 48–51, https://doi.org/10.1016/j.scriptamat.2013.10.001.

[43] S.J. Zinkle, P.J. Maziasz, R.E. Stoller, Dose dependence of the microstructural evolution in neutron-irradiated austenitic stainless steel, J. Nucl. Mater. 206 (1993) 266–286, https://doi.org/10.1016/0022-3115(93)90128-L.

[44] L.K. Mansur, Correlation of neutron and heavy-ion damage. II. The predicted temperature shift if swelling with changes in radiation dose rate, J. Nucl. Mater. 78 (1978) 156–160, https://doi.org/10.1016/0022-3115(78)90514-7.

[45] E. Getto, Z. Jiao, A.M. Monterrosa, K. Sun, G.S. Was, Effect of pre-implanted helium on void swelling evolution in self-ion irradiated HT9, J. Nucl. Mater. 462 (2015) 458–469, https://doi.org/10.1016/j.jnucmat.2015.01.045.

[46] F.A. Garner, W.G. Wolfer, A Model for the Evolution of Network Dislocation Density in Irradiated Metals, 1982, pp. 467–498.

[47] H.C. Chen, D.H. Li, R.D. Lui, H.F. Huang, J.J. Li, G.H. Lei, Q. Huang, L.M. Bao, L. Yan, X.T. Zhou, Z.Y. Zhu, Ion irradiation induced disappearance of dislocations in a nickel-based alloy, Nucl. Instrum. Methods Phys. Res. Sect. B Beam Interact. Mater. Atoms (2016), https://doi.org/10.1016/j.nimb.2016.04.030.

[48] M. Song, Y. Yang, M. Wang, W. Kuang, C.R. Lear, G.S. Was, Probing long-range ordering in nickel-base alloys with proton irradiation, Acta Mater. (2018), https://doi.org/10.1016/j.actamat.2018.06.043.

[49] L.J. Yu, E.A. Marquis, Precipitation in proton- and ion-irradiated alloy 625 plus, J. Nucl. Mater. 553 (2021), 153040, https://doi.org/10.1016/j.jnucmat.2021.153040.

[50] Z. Li, D.R. Trinkle, Mesoscale modeling of vacancy-mediated Si segregation near an edge dislocation in Ni under irradiation, Phys. Rev. B 95 (2017) 1–9, https://doi.org/10.1103/PhysRevB.95.144107.

[51] S.M. Corporation, Www.Specialmetals.Com, Inconel alloy 625 (2013) 1–28. SMC-066.

[52] ASME, B.P.V.C. Asme, II.B-2015 Nonferrous Material, 2015, https://doi.org/10.4324/9780203346822-16.

[53] K.H. Yano, M.J. Swenson, Y. Wu, J.P. Wharry, TEM in situ micropillar compression tests of ion irradiated oxide dispersion strengthened alloy, J. Nucl. Mater. 483 (2017), https://doi.org/10.1016/j.jnucmat.2016.10.049.

[54] T. Berglund, F. Meurling, Oxygen content in PM HIP 625 and its effect on toughness, hot isostatic press, HIP'17 10 (2019) 135–141, https://doi.org/10.21741/9781644900031-19.

[55] A. Sergi, R.H.U. Khan, M.M. Attallah, The role of powder atomisation route on the microstructure and mechanical properties of hot isostatically pressed Inconel 625, Mater. Sci. Eng. 808 (2021), 140950, https://doi.org/10.1016/j.msea.2021.140950.

[56] A. Lind, U. Bergenlid, Mechanical properties of hot isostatic pressed type 316LN steel after irradiation to 2.5 dpa, 58–59, Fusion Eng. Des. (2001) 713–717, https://doi.org/10.1016/S0920-3796(01)00541-5.

[57] A. Lind, U. Bergenlid, Mechanical properties of hot isostatic pressed type 316LN steel after irradiation, J. Nucl. Mater. (2000) 451–454, https://doi.org/10.1016/S0022-3115(00)00084-2, 283–287.

[58] I. Cieślik, M. Duchna, T. Płociński, E. Wyszkowska, A. Azarov, M. Zieniuk, Ion irradiation effect on the microstructure of Inconel 625 obtained by Selective Laser Melting and by the metallurgical process, Surf. Coating. Technol. 396 (2020), 125952, https://doi.org/10.1016/j.surfcoat.2020.125952.

[59] J.L. Straalsund, C.K. Day, Effect of neutron irradiation on the elastic constants of Type 304 stainless steel, Nucl. Technol. 20 (1973) 27–34, https://doi.org/10.13182/NT73-2.

[60] G.E. Lucas, The evolution of mechanical property change in irradiated austenitic stainless steels, J. Nucl. Mater. 206 (1993) 287–305, https://doi.org/10.1016/0022-3115(93)90129-M.

[61] L. Tan, J.T. Busby, Formulating the strength factor α for improved predictability of radiation hardening, J. Nucl. Mater. 465 (2015) 724–730, https://doi.org/10.1016/j.jnucmat.2015.07.009.

[62] M.J. Swenson, C.K. Dolph, J.P. Wharry, The effects of oxide evolution on mechanical properties in proton- and neutron-irradiated Fe-9%Cr ODS steel, J. Nucl. Mater. 479 (2016) 426–435, https://doi.org/10.1016/j.jnucmat.2016.07.022.

[63] R.E. Stoller, S.J. Zinkle, On the relationship between uniaxial yield strength and resolved shear stress in polycrystalline materials, 283–287, J. Nucl. Mater. (2000) 349–352, https://doi.org/10.1016/S0022-3115(00)00378-0.

[64] F. Kroupa, P.B. Hirsch, Elastic interaction between prismatic dislocation loops and straight dislocations, Discuss. Faraday Soc. 38 (1964) 49–55, https://doi.org/10.1039/DF9643800049.

[65] S.I. Golubov, A.V. Barashev, R.E. Stoller, Radiation damage theory, Compr. Nucl. Mater. (2012), https://doi.org/10.1016/B978-0-08-056033-5.00029-X.

[66] H. Wiedersich, On the theory of void formation during irradiation, Radiat. Eff. 12 (1972) 111–125, https://doi.org/10.1080/00337577208231128.

[67] A.A. Kohnert, L. Capolungo, Sink strength and dislocation bias of three-dimensional microstructures, Phys. Rev. Mater. 3 (2019), 53608, https://doi.org/10.1103/PhysRevMaterials.3.053608.

[68] M.J. Makin, Void nucleation during electron irradiation, Philos. Mag. A 25 (1972) 761–767, https://doi.org/10.1080/14786437208228908.

[69] J.E. Harbottle, The influence of dislocations on the nucleation of voids in Nickel, Philos. Mag. A 27 (1973) 147–157, https://doi.org/10.1080/14786437308228921.

[70] M.P. Surh, J.B. Sturgeon, W.G. Wolfer, Radiation swelling behavior and its dependence on temperature, dose rate, and dislocation structure evolution, J. Nucl. Mater. 336 (2005) 217–224, https://doi.org/10.1016/j.jnucmat.2004.09.016.

[71] L.K. Mansur, Unified theoretical analysis of experimental swelling data for irradiated austenitic and ferritic/martensitic alloys, Metall. Trans. A 12 (1990) 1021–1035.

[72] S.J. Zinkle, Radiation-induced effects on microstructure, Compr. Nucl. Mater. (2012), https://doi.org/10.1016/B978-0-08-056033-5.00003-3.

[73] H. Schroeder, H. Ullmaier, Helium and hydrogen effects on the embrittlement of iron- and nickel-based alloys, J. Nucl. Mater. (1991) 118–124, https://doi.org/10.1016/0022-3115(91)90025-3, 179–181.

[74] X. Zhang, K. Hattar, Y. Chen, L. Shao, J. Li, C. Sun, K. Yu, N. Li, M.L. Taheri, H. Wang, J. Wang, M. Nastasi, Radiation damage in nanostructured materials, Prog. Mater. Sci. 96 (2018) 217–321, https://doi.org/10.1016/j.pmatsci.2018.03.002.

[75] G. Ackland, Controlling radiation damage, Sci. Magna 327 (2010), https://doi.org/10.1126/science.1185988.

[76] I.J. Beyerlein, A. Caro, M.J. Demkowicz, N.A. Mara, A. Misra, B.P. Uberuaga, Radiation damage tolerant nanomaterials, Mater. Today 16 (2013) 443–449, https://doi.org/10.1016/j.mattod.2013.10.019.

[77] J. Li, C. Fan, J. Ding, S. Xue, Y. Chen, Q. Li, H. Wang, X. Zhang, In situ heavy ion irradiation studies of nanopore shrinkage and enhanced radiation tolerance of nanoporous Au, Sci. Rep. 7 (2017) 1–10, https://doi.org/10.1038/srep39484.

[78] E.M. Bringa, J.D. Monk, A. Caro, § A. Misra, L. Zepeda-Ruiz, M. Duchaineau, F. Abraham, M. Nastasi, S.T. Picraux, Y.Q. Wang, D. Farkas, Are nanoporous materials radiation resistant? Nano Lett. 12 (2012) 3351–3355, https://doi.org/10.1021/nl201383u.

[79] M. Jin, P. Cao, S. Yip, M.P. Short, Radiation damage reduction by grain-boundary biased defect migration in nanocrystalline Cu, Acta Mater. 155 (2018) 410–417, https://doi.org/10.1016/j.actamat.2018.05.071.

[80] B. Muntifering, S.J. Blair, C. Gong, A. Dunn, R. Dingreville, J. Qu, K. Hattar, Cavity evolution at grain boundaries as a function of radiation damage and thermal conditions in nanocrystalline nickel, Mater. Res. Lett. 4 (2016) 96–103, https://doi.org/10.1080/21663831.2015.1121165.

[81] B. Duan, C. Heintze, F. Bergner, A. Ulbricht, S. Akhmadaliev, E. Oñorbe, Y. de Carlan, T. Wang, The effect of the initial microstructure in terms of sink strength on the ion-irradiation-induced hardening of ODS alloys studied by nanoindentation, J. Nucl. Mater. 495 (2017) 118–127, https://doi.org/10.1016/j.jnucmat.2017.08.014.

[82] C. Heintze, I. Hilger, F. Bergner, T. Weissgärber, B. Kieback, Nanoindentation of single- (Fe) and dual-beam (Fe and He) ion-irradiated ODS Fe-14Cr-based alloys: effect of the initial microstructure on irradiation-induced hardening, J. Nucl. Mater. 518 (2019) 1–10, https://doi.org/10.1016/j.jnucmat.2019.02.037.

[83] Y. Bazarbayev, M. Kattoura, K.S. Mao, J. Song, V.K. Vasudevan, J.P. Wharry, Effects of corrosion-inhibiting surface treatments on irradiated microstructure development in Ni-base alloy 718, J. Nucl. Mater. 512 (2018) 276–287, https://doi.org/10.1016/j.jnucmat.2018.10.006.